Spin dynamics of magnetic resonance with parametric modulation in a potassium vapor cell*

Rui Zhang(张锐)[1,2], Zhi-Guo Wang(汪之国)[1,3], Xiang Peng(彭翔)[2,†], Wen-Hao Li(黎文浩)[2], Song-Jian Li(李松健)[2], and Hong Guo(郭弘)[1,2,‡]

[1] College of Science, and Interdisciplinary Center for Quantum Information, National University of Defense Technology, Changsha 410073, China
[2] State Key Laboratory of Advanced Optical Communication Systems and Networks, School of Electronics Engineering and Computer Science, and Center for Quantum Information Technology, Peking University, Beijing 100871, China
[3] College of Optoelectronic Science and Engineering, National University of Defense Technology, Changsha 410073, China

(Received 16 October 2016; revised manuscript received 23 December 2016; published online 18 January 2017)

A typical magnetic-resonance scheme employs a static bias magnetic field and an orthogonal driving magnetic field oscillating at the Larmor frequency, at which the atomic polarization precesses around the static magnetic field. Here we demonstrate both theoretically and experimentally the variations of the resonance condition and the spin precession dynamics resulting from the parametric modulation of the bias field. We show that the driving magnetic field with the frequency detuned by different harmonics of the parametric modulation frequency can lead to resonance as well. Also, a series of frequency sidebands centered at the driving frequency and spaced by the parametric modulation frequency can be observed in the precession of the atomic polarization. We further show that the resonant amplitudes of the sidebands can be controlled by varying the ratio between the amplitude and the frequency of the parametric modulation. These effects could be used in different atomic magnetometry applications.

Keywords: atomic magnetometer, magnetic resonance, parametric modulation

PACS: 07.55.Ge, 32.30.Dx, 32.10.Dk, 32.80.Xx **DOI:** 10.1088/1674-1056/26/3/030701

1. Introduction

Magnetic resonance in an alkali metal vapor cell typically involves optical detection of the ground-state Zeeman resonance in optically polarized alkali atoms. As it paves the way for highly sensitive, cryogenic-cooling-free magnetic field detection, it is commonly used in atomic magnetometers (AMs).[1] In those applications, the resonance condition that a driving magnetic field, applied transverse to a static bias magnetic field, oscillates at the Larmor frequency is required to achieve sensitive detection of magnetic fields. The resonance frequency is proportional to the bias magnetic field up to a scaling factor (gyromagnetic ratio), which is the core of scalar AMs.[2] It also leads to the fact that radio-frequency (RF) AMs can be sensitive to oscillating magnetic fields in the vicinity of the Larmor frequency.[3]

However, reference [4] shows that AMs could also be resonant even if the driving frequency ω is different from the Larmor frequency ω_0, as long as a small magnetic field modulation at frequency $|\omega_0 - \omega|$ is applied along the direction of the bias magnetic field. Furthermore, enhancement of the signal response of AMs near $|\omega_0 - \omega|$ is demonstrated with the detection of the small magnetic field modulation, even if $|\omega_0 - \omega|$ is beyond the original cutoff frequency. Similarly, this effect has the potential for enabling detection of either the bias or the driving magnetic field. Since the magnetic field modulation along the leading field direction provides extra parameters, the detections may exhibit novel behaviors. For this purpose, knowledge about the spin dynamics in this scheme with arbitrary modulation amplitude is needed.

Even though large magnetic field modulations were introduced in many references, their influences on spin dynamics have not been studied thoroughly. In zero-field level-crossing-resonance magnetometers, references [5]–[10] applied a large-amplitude RF magnetic field for noise suppression, and reference [11] further introduced another RF field for vector-mode operation. But the setups of these references are different from the present one. The setups in Refs. [12] and [13] are almost the same as that in Ref. [4], in which the parametric modulation is applied to facilitate the optical detection of the driving magnetic field, but the driving field is treated as a quasistatic field there. By analogy with the results of Ref. [6], Eklund[13] found that a parametric modulation at a subharmonic of the Larmor frequency would also lead to resonance, but obviously this may not be precise enough for driving field of high frequencies.

In this work, we analyze the influence of a longitudinal sinusoidal magnetic field modulation on spin dynamics in the typical magnetic resonance setup, which is valid for large-

*Project supported by the National Science Fund for Distinguished Young Scholars of China (Grant No. 61225003), the National Natural Science Foundation of China (Grant Nos. 61531003 and 61571018), and the National High Technology Research and Development Program of China.

†Corresponding author. E-mail: xiangpeng@pku.edu.cn
‡Corresponding author. E-mail: hongguo@pku.edu.cn

© 2017 Chinese Physical Society and IOP Publishing Ltd

amplitude parametric modulations and high-frequency driving fields. We show that high-order frequency sidebands occur in the precession of atomic polarization and modulation at subharmonic of $|\omega_0 \pm \omega|$ can also lead to resonance. We experimentally demonstrate these effects in a potassium vapor cell.

2. Theory

We study the spin dynamics of optically pumped alkali vapors in the typical magnetic-resonance scheme that involves an extra parametric modulation on the bias magnetic field. We analyze perturbatively the time-dependent Bloch equations and show that compared with the small parametric modulation case, the large-amplitude modulation leads to higher-order sidebands in the detected magnetic resonance signal, more choices of resonant driving frequencies, and nonlinear spin dynamics in response to the modulation amplitude.

The coordinate system we used for the analysis of the spin dynamics is shown in Fig. 1. A static bias magnetic field B_0 is applied along the z axis, superposed with a modulation $B_c \cos \omega_c t$ in the same direction. A near-resonant, circularly polarized pump beam creates a long-lived polarization parallel to the bias magnetic field in the atomic ground state. Part of the polarization is tilted away from the pumping axis by a driving field $2B_a \cos(\omega t)$ along the x axis, and subsequently the tilted part precesses around the bias field. As we are interested in the transverse component of the atomic spins, the optical rotation of a far-detuned, linearly polarized probe light is detected.

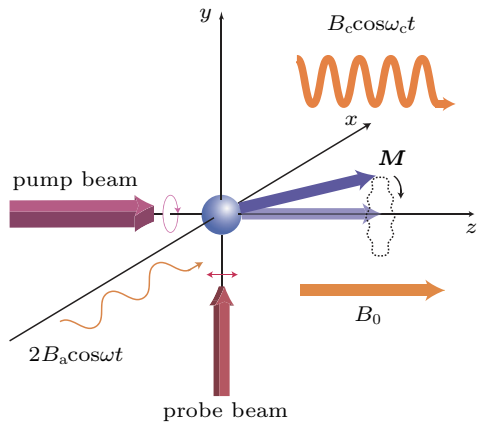


Fig. 1. (color online) Principle of the parametric-modulated magnetic resonance. $2B_a \cos \omega t$: driving magnetic field, B_0: static bias magnetic field, $B_c \cos \omega_c t$: longitudinal magnetic modulation.

During the interactions of the pump beam and the magnetic field, the spin dynamics can be described by the Bloch equation[14]

$$\frac{\mathrm{d}\boldsymbol{M}}{\mathrm{d}t} = \frac{\boldsymbol{M}_0 - \boldsymbol{M}}{T_\mathrm{P}} - \left(\frac{M_x}{T_2}\hat{\boldsymbol{e}}_x + \frac{M_y}{T_2}\hat{\boldsymbol{e}}_y + \frac{M_z}{T_1}\hat{\boldsymbol{e}}_z\right) + \gamma \boldsymbol{M} \times \boldsymbol{B}, \quad (1)$$

where $\boldsymbol{M} = (M_x, M_y, M_z)^\mathrm{T}$ is the magnetization vector, $\boldsymbol{M}_0$ is the equilibrium magnetization induced by the optical pumping, T_P is the time constant for the pumping process, T_1 and T_2 are the longitudinal relaxation time and the transverse relaxation time, respectively, γ is the gyromagnetic ratio, and $\boldsymbol{B} = (B_x, B_y, B_z)^\mathrm{T} = (2B_a \cos \omega t, 0, B_0 + B_c \cos \omega_c t)^\mathrm{T}$ is the total magnetic field applied to the atomic ensemble. For brevity, we denote $1/\tau_1 = 1/T_\mathrm{P} + 1/T_1$, $1/\tau_2 = 1/T_\mathrm{P} + 1/T_2$, $M_0' = M_0 \tau_1 / T_\mathrm{P}$, $\omega_0 = \gamma B_0$, $\omega_1 = \gamma B_c$, and $\beta = \omega_1/\omega_c$.

In practice, γB_a is normally slow compared with the combined transverse relaxation rate $1/\tau_2$. Without the longitudinal modulation, the scheme presented in Fig. 1 is widely used in RF AMs and scalar AMs. In RF AMs, since $2B_a \cos \omega t$ is the quantity to be measured, the condition above is satisfied generally. As for scalar AMs, a large driving field with γB_a comparable to $1/\tau_2$ would lead to significant RF broadening of the resonance line and decrease the sensitivity of the AMs,[15] which should be avoided typically. As a consequence, the driving field could be treated as a perturbation. The perturbative expansion of $\boldsymbol{M}$ in $\gamma B_a \tau_2$ is

$$M_\alpha = M_\alpha^{(0)} + M_\alpha^{(1)} + M_\alpha^{(2)} + \cdots, \quad (\alpha = x, y, z), \quad (2)$$

where $M_\alpha^{(k)}$ is the k-th order term. We could substitute Eq. (2) and other parameters into Eq. (1),

$$\frac{\mathrm{d}}{\mathrm{d}t}M_x^{(k)} + \frac{1}{\tau_2}M_x^{(k)} - (\omega_0 + \omega_1 \cos \omega_c t) M_y^{(k)} = 0, \quad (3a)$$

$$\frac{\mathrm{d}}{\mathrm{d}t}M_y^{(k)} + \frac{1}{\tau_2}M_y^{(k)} + (\omega_0 + \omega_1 \cos \omega_c t) M_x^{(k)} - 2\gamma B_a \cos \omega t \, M_z^{(k-1)} = 0, \quad (3b)$$

$$\frac{\mathrm{d}}{\mathrm{d}t}M_z^{(k)} + \frac{1}{\tau_1}M_z^{(k)} - \delta_{k,0}\frac{1}{\tau_1}M_0' + 2\gamma B_a \cos \omega t \, M_y^{(k-1)} = 0. \quad (3c)$$

We define $M_\alpha^{(k)} = 0$ for $k < 0$.

Defining $M_+ = M_x + \mathrm{i}M_y$, we can solve Eq. (2) with a testing solution

$$M_+^{(k)} = (\lambda_1^{(k)} \mathrm{e}^{-\mathrm{i}\omega t} + \lambda_2^{(k)} \mathrm{e}^{\mathrm{i}\omega t}) \mathrm{e}^{-t/\tau_2} \mathrm{e}^{-\mathrm{i}(\omega_0 t + \beta \sin \omega_c t)}.$$

In the stationary state, M_z is $M_z \approx M_0'$ to the first order, and M_+ to the second order is

$$M_+ \approx \mathrm{i}\gamma B_a M_0' \sum_{q=-\infty}^{\infty} \sum_{p=-\infty}^{\infty} \mathrm{J}_q(\beta) \mathrm{J}_{q-p}(\beta) \mathrm{e}^{\mathrm{i}p\omega_c t} \times \left[\Xi_{q,-1} \mathrm{e}^{-\mathrm{i}\omega t} + \Xi_{q,1} \mathrm{e}^{\mathrm{i}\omega t}\right], \quad (4)$$

where $\Xi_{m,n} = 1/[1/\tau_2 + \mathrm{i}(\omega_0 + m\omega_c + n\omega)]$. In this process, Jacobi–Anger expansion $\mathrm{e}^{\pm \mathrm{i}(\beta \sin \omega_c t)} = \sum_{q=-\infty}^{\infty} \mathrm{J}_q(\beta) \mathrm{e}^{\pm \mathrm{i}q\omega_c t}$ is employed, where J_q is the q-th Bessel function of the first kind. When $B_c = 0$, equation (4) is reduced to the form that is known for the case without longitudinal modulation

$$M_+ \approx \frac{\mathrm{i}\gamma B_a M_0' \mathrm{e}^{-\mathrm{i}\omega t}}{1/\tau_2 + \mathrm{i}(\omega_0 - \omega)} + \frac{\mathrm{i}\gamma B_a M_0' \mathrm{e}^{\mathrm{i}\omega t}}{1/\tau_2 + \mathrm{i}(\omega_0 + \omega)}. \quad (5)$$

Making a comparison of the positive frequency parts $\mathrm{e}^{-\mathrm{i}\omega t}$ in Eqs. (4) and (5), we find that when the longitudinal

modulation is applied, an infinite number of sidebands spaced by ω_c are generated on both sides of the driving frequency ω in the transverse spin. Additionally, all of these sidebands would be resonant simultaneously for ω that differs from ω_0 by harmonics of ω_c, with the resonance linewidth unchanged. The resonant amplitude of each sideband is still proportional to the driving amplitude B_a, but its relation with the normalized modulation amplitude β is nonlinear and is described by the Bessel function.

The resonances at $\omega = \pm(\omega_0 + q\omega_c)$ with $|q| > 1$ and the sidebands at frequencies $\pm\omega + p\omega_c$ with $|p| > 1$ predicted in Eq. (4) would only be obvious for large modulations. In the limit of small modulation, i.e., $\beta \ll 1$, $J_q(\beta)$ is proportional to $\beta^{|q|}$. As a result, the amplitudes of the $|q| > 1$ and $|p| > 1$ terms in Eq. (4) are proportional to the second or higher orders of β, which are too small to be observed.

As for the detection of the transverse spin, the optical rotation of the probe beam in Fig. 1 is proportional to M_y, the projection of the magnetization vector along the propagation direction of the probe beam, and is usually converted linearly to an electric signal in the case of small optical-rotation angle.[15] In other words, the electric signal from the polarimeter is proportional to M_y. As the signal is usually analyzed with a lock-in amplifier, it is necessary to obtain the frequency characteristics of M_y. In general, a stationary magnetization vector could be expanded into Fourier series

$$M_\alpha = \sum_m \sum_n C^\alpha_{m,n} e^{i(m\omega_c + n\omega)t}, \quad (\alpha = x, y, z), \tag{6}$$

where $C^\alpha_{m,n}$ is the complex amplitude of the Fourier component at angular frequency $m\omega_c + n\omega$ of M_α. If the electric signal is demodulated at $m\omega_c + n\omega$ to get the amplitude of this frequency component, the result is proportional to $|C^y_{m,n}|$. Comparing Eq. (4) with Eq. (6), we find that for $n \geq 0$,

$$C^y_{m,n} \approx \frac{1}{2}\delta_{n,1}\gamma M'_0 B_a \times \sum_{q=-\infty}^{\infty} J_q(\beta) J_{q-m}(\beta) \times \left[\Xi_{q,1} + \Xi^*_{-q,-1}(-1)^m\right], \tag{7}$$

where Θ^* represents the complex conjugate of Θ. The expression of $C^y_{m,n}$ for $n < 0$ can be deduced easily from Eq. (7) with the relation $C^y_{m,n} = C^{y*}_{-m,-n}$.

It is obvious that M_y inherits the properties of M_+ discussed above. As a result, there are a number of sidebands spaced by ω_c in the detected signal. When the signal is demodulated by a lock-in amplifier to extract the amplitudes of certain sidebands, the results would get to local maximums if ω is detuned from ω_0 by harmonics of ω_c, which satisfies the resonance condition. The demodulation results at resonance are proportional to the amplitude of the driving field, but are nonlinear to the amplitude of the parametric modulation field.

3. Experimental setup

A schematic of the experimental setup is shown in Fig. 2. We use a 20 mm diameter cross-shape glass cell as the magnetic sensor, which contains natural abundance potassium, 750 torr of helium as the buffer gas, and 50 torr of nitrogen as the quenching gas. Gyromagnetic ratio of potassium is $\gamma = 2\pi \times 7$ Hz/nT. The cell is placed in an oven and heated by a resistive heater using alternating current (AC) at 20 kHz. The heater is turned off during measurements. The temperature of the cell is maintained at 95 °C to obtain a sufficient signal-to-noise ratio. The cell, oven, and three-axis Helmholtz coils are placed in a seven-layer permalloy magnetic shield. The z-axis and the x-axis Helmholtz coils, driven by a signal generator in a digital lock-in amplifier (Zurich Instruments HF2LI), apply $B_0 + B_c \cos \omega_c t$ along the z axis and a small-amplitude oscillating field $2B_a \cos \omega t$ along the x axis, respectively. The y-axis Helmholtz coil is driven by a current source (Keysight Technologies B2900). The residual magnetic field inside the shield is cancelled before operation. The calibration constants of the Helmholtz coils are calibrated with a fluxgate magnetometer in the case of a direct current (DC) driving signal. With the help of a pickup coil, we verify that the Helmholtz coils have almost flat frequency responses in the frequency range from DC to 2.5 kHz, which covers the modulation frequency in the subsequent experiments. Therefore, the strengths of the oscillating magnetic fields, B_c and B_a, which oscillate at frequencies in the flat-frequency-response regime of the coils, can be reasonably estimated with the calibration constants measured with the DC signal.

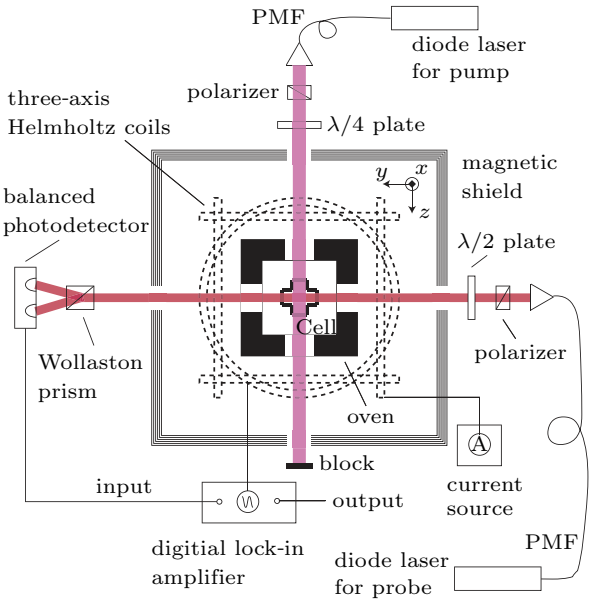


Fig. 2. (color online) Schematic of the experimental setup. PMF: polarization maintaining optical fiber.

A circularly polarized, 24 mm diameter pump laser is frequency locked to the central crossover resonance of potassium

D1 line and creates a spin polarization of K atoms along the z axis. A linearly polarized, 9 mm diameter probe laser is detuned 33 GHz away from the D2 resonance to the high-frequency side, whose optical-rotation angle is proportional to the y component of the magnetization vector M_y. Then a polarimeter composed of a Wollaston prism and a balanced photodetector generates an electric signal proportional to the rotation angle of the probe light, which is subsequently demodulated by the digital lock-in amplifier to extract the amplitudes of certain sidebands. For example, as the signal is proportional to M_y, when it is demodulated at $|m\omega_c + n\omega|$, the output is in proportion to $|C^y_{m,n}|$ in Eq. (7), i.e., the amplitude of the Fourier component at angular frequency $m\omega_c + n\omega$ of M_y. To avoid extra optical power broadening of the resonance lines, the power densities of the pump and the probe beams are set to relatively low levels ($I_{\rm pump} \approx 0.13$ mW/cm^2, $I_{\rm probe} \approx 0.70 \sim 1.1$ mW/cm^2). τ_2 varies slightly between experiments because of the different $I_{\rm probe}$.

4. Results and discussion

Theoretical analysis in Section 2 indicates that there are various resonant driving frequencies at which the amplitudes of the sidebands in the detected signal get to local maximums simultaneously, and that these resonant amplitudes are proportional to the driving amplitude and nonlinear to the normalized modulation amplitude. To confirm these predictions, we compare the experimental and theoretical spin dynamics of the potassium vapor in the setup shown in Fig. 2. The measured resonance conditions in the experiments are in good agreement with the theoretical predictions from Eq. (7). Then, we test the consistency of the resonant amplitudes of the sidebands between the theory and the experiments at various modulation amplitudes. Finally, we find out the validity region of the approximation condition used in the perturbation treatment.

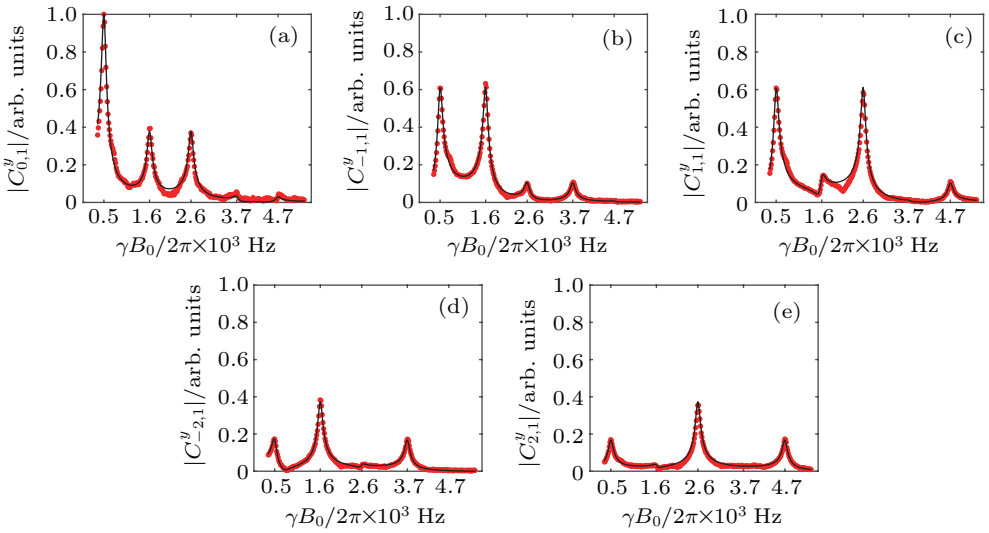


Fig. 3. (color online) $|C^y_{m,1}|$ as a function of γB_0. Red points indicate experimental results, while black solid lines overlaying the data are fitted curves described in the text.

Equation (7) shows that it would be resonant as long as the denominator of a term gets to the minimum, i.e., $\omega_0 \pm q\omega_c \pm \omega = 0$ for certain values of q. To verify these resonant conditions, we could scan either ω_0, ω_c, or ω to obtain the resonance spectra. Among them, scanning ω_0, i.e., γB_0, is most convenient as it would not change other parameters like the frequencies of the sidebands and the normalized modulation amplitude β. We show in Fig. 3 the amplitudes of different sidebands in M_y as a function of γB_0. ω_c and ω are set to $2\pi \times 2.1$ kHz and $2\pi \times 0.5$ kHz, respectively, which are not changed in all the following experiments. To make the resonance distinct, we choose a relatively large modulation amplitude with β equaling 1.05. The driving amplitude B_a is set to 108 pT. Figures 3(a)–3(e) correspond to the sidebands at angular frequencies ω, $|\omega \mp \omega_c|$, and $|\omega \mp 2\omega_c|$, respectively, and the amplitude-normalizing factor is the same among the sub-figures. The experimental results are in good agreement with the theoretical predictions from Eq. (7), with fitted value of τ_2 equaling 2.68 ms. Thus $\gamma B_a \tau_2$ is 0.013 here. In addition to the conventional resonant condition $\gamma B_0 = \omega$, there are also peaks with the same linewidth when γB_0 equals $|\omega \mp \omega_c|$ and $|\omega \mp 2\omega_c|$, corresponding to the modified resonant driving frequencies of $|\gamma B_0 - \omega_c|$ and $|\gamma B_0 - 2\omega_c|$, respectively. The resonances at $\gamma B_0 = |\omega \mp 2\omega_c|$ that are negligible in the small modulation case[4] are now comparable in amplitudes with those at $\gamma B_0 = |\omega \mp \omega_c|$. These resonance conditions are quite different from those in the low driving frequency case.[13]

Figure 4 presents the amplitudes of several sidebands as a function of the normalized modulation amplitude β at resonant conditions of (a) $\gamma B_0 = \omega$ and (b) $\gamma B_0 = \omega + \omega_c$.

The amplitude-normalizing factor is the same among the subfigures. As ω_c is fixed at $2\pi \times 2.1$ kHz, we scan the modulation amplitude B_c here. Under the condition $\gamma B_0 = \omega + \omega_c$, the curves representing $|C^y_{2,1}|$ and $|C^y_{0,1}|$ almost completely overlap, so $|C^y_{2,1}|$ is not presented in Fig. 4(b). τ_2 is measured to be 2.27 ms,[4] and B_a is set to 108 pT, corresponding to $\gamma B_a \tau_2 = 0.011$. This shows that the experimental results can be well described by the theory (Eq. (7)). The relation between the resonant amplitudes and β is nonlinear, and all of these amplitudes have their maxima. Taking the case of $\gamma B_0 = \omega$ for example, the maximal experimental amplitudes of these three sidebands occur at β equaling 0, 1.08, and 3.55, respectively, with amplitudes ratio 1: 0.306: 0.153. In other words, with the optimal β, $|C^y_{\pm1,1}|$ and $|C^y_{\pm2,1}|$ under the resonant condition $\gamma B_0 = \omega$ are of the same order of magnitude as $|C^y_{0,1}|$ in the non-modulation case, which makes it feasible to use these sidebands in different magnetometry schemes. For example, measuring the sideband at frequency $|\omega + \omega_c|$ may help to improve the magnetic detection sensitivities as there are less technical noises at higher frequencies, and measuring the sideband at frequency $|\omega - \omega_c|$ may reduce the requirement of detector bandwidth in some applications as it can shift the detected signal to lower frequencies. The situation is similar when γB_0 equals $\omega + \omega_c$.

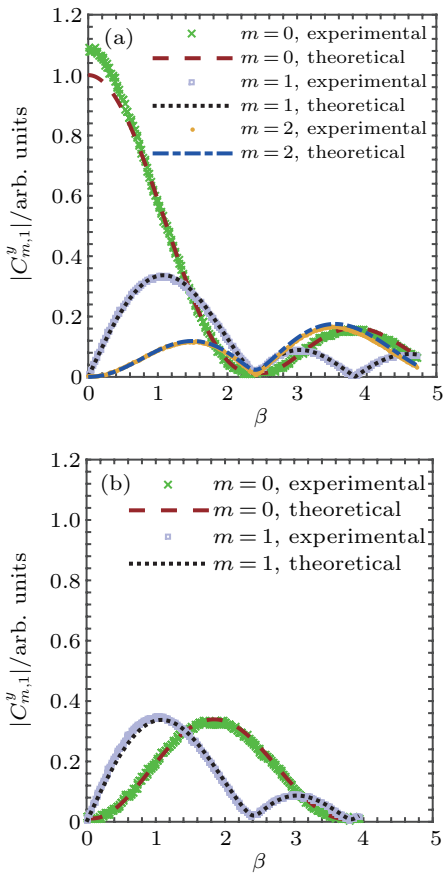


Fig. 4. (color online) Measured $|C^y_{m,1}|$ as a function of β for different m, showing comparison with the approximate theoretical results (Eq. (7)). The resonance conditions are (a) $\gamma B_0 = \omega$ and (b) $\gamma B_0 = \omega + \omega_c$.

An interesting effect shown in Fig. 4(a) is that the amplitudes of these three sidebands all reach their minima at $\beta = 2.40$. Equation (7) shows that when $\gamma B_0 = \omega$, the terms with the smallest denominator in $|C^y_{0,1}|$, $|C^y_{1,1}|$, and $|C^y_{2,1}|$ are proportional to $J_0^2(\beta)$, $J_0(\beta)J_1(\beta)$, and $J_0(\beta)J_2(\beta)$, respectively. All of these terms vanish at $\beta = 2.405$ as $J_0(2.405) \approx 0$, leading to the minima in these curves. Because of the induced inductance and capacitance, the frequency responses of the coils are not flat, which should be calibrated in experiments.[16,17] As the minima of $|C^y_{m,1}|$ are easy to distinguish and give a rigid connection between the amplitude and the frequency of the modulation field, it provides a simple way to calibrate the frequency responses of the coils. Finding the minima could be done automatically by applying a low-frequency amplitude modulation to the voltage signal that drives the coils and then employing the phase sensitive detection to get a dispersion error signal for feedback control.

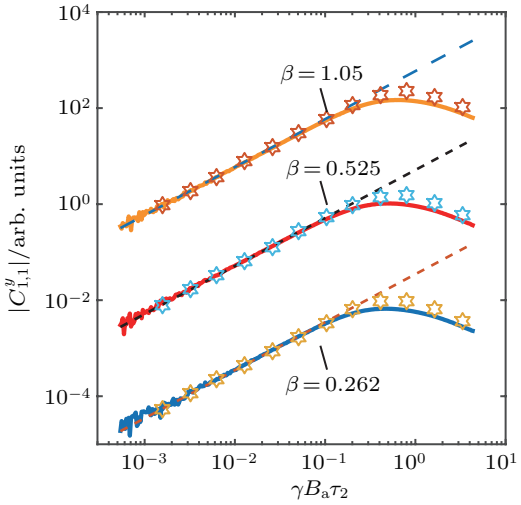


Fig. 5. (color online) $|C^y_{1,1}|$ at resonant condition $\gamma B_0 = \omega$ as a function of $\gamma B_a \tau_2$ for different β. The solid lines represent measured data. The dashed lines represent $|C^y_{1,1}|$ from Eq. (7). The hexagonal markers represent the results obtained numerically from the time-dependent Bloch equation Eq. (1). The data groups from bottom to top correspond to β equaling 0.262, 0.525, and 1.05, respectively, and they are vertically shifted for clarity.

As equation (7) is a result of the second-order perturbation theory, its validity region should be pointed out. In other words, we should discover the range of $\gamma B_a \tau_2$ in which the perturbation terms of orders higher than 2 in M_y could be omitted. Equation (7) implies that the amplitude of each sideband in M_y is proportional to B_a. This linearity could be used to judge the validity of the approximation. Figure 5 shows $|C^y_{1,1}|$ as a function of $\gamma B_a \tau_2$ for different β, with B_0 fixed at ω/γ. The solid lines are the experimental results, the dashed lines represent the theoretical predictions from Eq. (7), and the hexagonal markers are the numerical results obtained from the integrated time-dependent Bloch equations using the Runge–Kutta method. τ_2 here is measured to be 2.27 ms. τ_1 used

in the numerical calculation is set to twice τ_2, as it is typically slightly larger than τ_2.[15] From Fig. 5, we can find that when $\gamma B_a \tau_2 < 0.1$, the experimental results coincide with fittings from Eq. (7). Otherwise, the experimental results are no longer linear with B_a and share the same trend with the numerical results. It suggests that the approximation is valid in the range of $\gamma B_a \tau_2 < 0.1$. Since $\gamma B_a \tau_2$ is set to be around 0.01 in the previous experiments, it is valid to fit the experimental results with Eq. (7).

5. Conclusion

We focus on the transverse spin dynamics in a typical magnetic-resonance scheme that involves an extra parametric modulation on the bias field. With the help of perturbation analysis and experiments in a potassium vapor at 95 °C, we find that a number of sidebands spaced by the modulation frequency ω_c are generated on both sides of the driving frequency ω, and that all these sidebands would be resonant simultaneously when ω differs from the traditional magnetic resonance frequency by harmonics of ω_c, with the resonance linewidth unchanged. In this setup, the sidebands and resonance conditions with orders higher than one would only be obvious for large modulation. Besides, the resonant amplitudes of the sidebands are proportional to the driving amplitude while nonlinear to the normalized modulation amplitude. Under the optimal modulation condition, the resonant amplitudes of some low-order sidebands are comparable to that of the traditional magnetic resonance.

As a result, these new generated sidebands could also be used in AMs, and may help to improve the sensitivities by measuring $\omega + \omega_c$ sideband if the original frequency ω is low, or reduce the requirement of the detector bandwidth by measuring $\omega - \omega_c$ sideband if ω is too high. Based on the nonlinear dependence of the resonant amplitude on the normalized modulation amplitudes, a method of frequency response calibration for the magnetic coils is proposed. Although we only demonstrate these effects in a potassium vapor, the analysis could be extended to other alkali-metal atoms. Future work includes study in similar spin dynamics in spin-exchange-relaxation-free (SERF) regime.[1,18]

Acknowledgment

We acknowledge Bin Luo for helpful discussions, Tianliang Qu, Yuanzhi Zhan, and Sheng Li for carefully reading the manuscript, and Yucheng Yang for contributions at the early stages of the project.

References

[1] Budker D and Romalis M 2007 *Nat. Phys.* **3** 227
[2] Bloom A L 1962 *Appl. Opt.* **1** 61
[3] Savukov I M, Seltzer S J, Romalis M V and Sauer K L 2005 *Phys. Rev. Lett.* **95** 063004
[4] Terao A, Ban K, Ichihara S, Mizutani N and Kobayashi T 2013 *Phys. Rev. A* **88** 063413
[5] Dupont-Roc J, Haroche S and Cohen-Tannoudji C 1969 *Phys. Lett. A* **28** 638
[6] Cohen-Tannoudji C, Dupont-Roc J, Haroche S and Laloë F 1970 *Rev. Phys. Appl. (Paris)* **5** 95
[7] Slocum R and Marton B 1973 *IEEE Transactions on Magnetics* **9** 221
[8] Li Z, Wakai R T and Walker T G 2006 *Appl. Phys. Lett.* **89** 134105
[9] Li S G, Xu Y F, Wang Z Y, Liu Y X and Lin Q 2009 *Chin. Phys. Lett.* **26** 067805
[10] Shah V and Romalis M V 2009 *Phys. Rev. A* **80** 013416
[11] Dupont-Roc J 1970 *Rev. Phys. Appl.* **5** 853
[12] Grover B C, Kanegsberg E, Mark J G and Meyer R L 1979 (U.S. Patent) 4 157 495 [1979-06-05]
[13] Eklund E J 2008 *Microgyroscope based on spin-polarized nuclei* (Ph.D. Dissertation) (Irvine: University of California, Irvine)
[14] Bloch F 1946 *Phys. Rev.* **70** 460
[15] Seltzer J S 2008 *Developments in alkali-metal atomic magnetometry* (Ph.D. Dissertation) (Princeton: Princeton University)
[16] Ledbetter M P, Acosta V M, Rochester S M, Budker D, Pustelny S and Yashchuk V V 2007 *Phys. Rev. A* **75** 023405
[17] Lu J X, Qian Z, Fang J C and Quan W 2016 *Appl. Phys. B* **122** 1
[18] Happer W and Tam A C 1977 *Phys. Rev. A* **16** 1877